Fehse, Marcus, Hogan, Matteo P., Pang, Sally Hiu-Tung, Blackman, Oliver, Kelder, Erik M., Longo, Alessandro and Alfredsson, Maria (2020) *Monitoring and quantifying morphological and structural changes in electrode materials under operando conditions.* Journal of Power Sources, 478 . ISSN 0378-7753.

Monitoring and quantifying morphological and structural changes in electrode materials under *operando* conditions

Marcus Fehse [a,b,c,*], Matteo P. Hogan [d], Sally Hiu-Tung Pang [d], Oliver Blackman [d], Erik M. Kelder [a,c], Alessandro Longo [e,f], Maria Alfredsson [d,c]

[a] *Faculty of Applied Sciences, Delft University of Technology, Delft, the Netherlands*
[b] *CIC Energigune, Parque Tecnológico de Álava, Albert Einstein 48, ED. CIC 01510, Miñano, Spain*
[c] *Alistore European Research Institute, Université de Picardie Jules Verne, 33 Rue Saint Leu, 80039, Amiens Cedex, France*
[d] *School of Physical Sciences, University of Kent, CT2 7NH, UK*
[e] *ESRF - the European Synchrotron, CS 40220, 38043, Grenoble Cedex 9, France*
[f] *Istituto per Lo Studio dei Materiali Nanostrutturati (ISMN)-CNR, UOS Palermo, Via Ugo La Malfa, 153, 90146, Palermo, Italy*

HIGHLIGHTS

- Simultaneous acquisition of SAXS and XAS spectra under *operando* conditions.
- SAXS-XANES approach first time applied in the field of energy storage materials.
- Jointly monitor electronic and nano structural changes under operando conditions.
- Identify state of charge and quantify morphological changes.
- Improved reversibility of Sr-doped vs. non-doped Fe_2O_3 during first cycle.

GRAPHICAL ABSTRACT
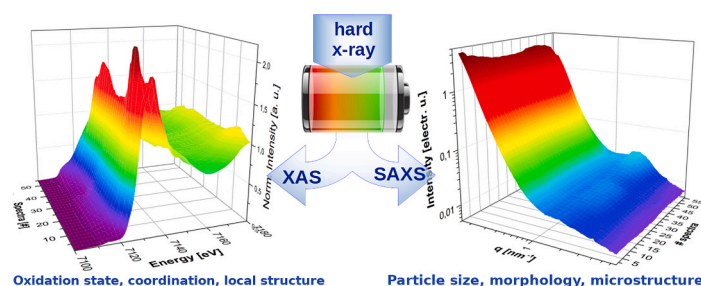
Oxidation state, coordination, local structure

Particle size, morphology, microstructure

ARTICLE INFO

ABSTRACT

X-ray absorption and small-angle x-ray scattering spectra were simultaneously acquired under *operando* conditions in a joined technique approach, for the first time applied in the field of energy storage materials. This approach allows one to closely follow the electronic and local structure evolution, as well as monitor and quantify the morphological and nanostructural changes occurring during electrochemical cycling. Here we demonstrate its potential on the example of doped and non-doped Fe_2O_3 anode material vs. Li. Our results reveal that upon discharge Fe^{3+} is gradually reduced to the metallic state and segregated as nanoparticles. For the relithiation reaction, upon subsequent charge, we observe improved reversibility for the Sr-doped compared to non-doped and Ca-doped Fe_2O_3. We highlight that this combined technique approach is a reliable, facile and powerful tool to investigate electrode materials under realistic cycling condition. It provides an unbiased and holistic picture of the morphological and structural changes occurring during operation, which allows for adequate material tailoring.

---

* Corresponding author. Faculty of Applied Sciences, Delft University of Technology, Delft, Netherlands.
  E-mail address: marcus.fehse@umontpellier.fr (M. Fehse).

1. Introduction

Operando measurements for characterising battery materials have become very popular, since they allow monitoring of diverse electrode material properties under realistic conditions, providing a reliable and holistic picture of the internal mechanisms and processes occurring during the electrochemical reaction [1]. In this regard, x-ray absorption spectroscopy (XAS) is a particularly informative and hence attractive technique. It probes element-specific the electronic and next-neighbour structure, thus providing insights on the evolution of oxidation state and local structural transformations. XAS is especially useful for battery materials that undergo strong nanostructuring upon electrochemical reaction, which impedes the use of x-ray diffraction (XRD) for their analysis [2]. Furthermore, it has been shown that *operando* XAS can be applied to explore the multistep reaction mechanism and reveal reaction intermediates [3,4]. Moreover, XAS analysis can be coupled with imaging technique to gain qualitative information on the electrode morphology under *operando* conditions [5,6].

Considerably less well-known, in the field of battery materials, is the small-angle x-ray Scattering (SAXS) technique. In this technique the signal intensity arises from scattering length density fluctuations in the beampath, which permits the probing of morphology and structure in the mesoscopic length scale, typically 1–100 nm [7,8]. Compared to conventionally used microscopy (SEM, TEM) SAXS offers several intrinsic advantages for morphological and structural examination of electrode materials. Firstly, it allows probing of large sampling size which reduces the bias. Secondly it offers the possibility to carry out bulk sensitive quantitative analysis and thirdly it avoids the problem of sample beam-damage. The possibility to extract quantitative structural parameters such as average particle size and their packing density is an unique asset of this technique. Moreover, SAXS can be comparatively easy applied under *in situ* or *operando* conditions, leading to increased precision, reliability and traceability of the experimental findings. Last but not least, carrying out continuous *operando* measurement in a sealed electrochemical cell circumvents problems of sample relaxation, contamination or short circuiting, which are inherent to *ex situ* or *post mortem* studies [1,9].

In previous battery-related studies the SAXS technique has been primarily applied to investigate polymer-electrolyte or porous carbon-based electrode materials [10–16]. Recently however, several studies have demonstrated its versatility to monitor changes of morphology and microstructure in conversion and alloy-type electrode materials [17–21]. Such post-lithium ion electrode materials are of great interest to the battery research community, since they hold the promise to overcome the intrinsically low capacity of conventional insertion type electrode materials. The large capacity of conversion and alloy-type electrode materials is based on the complete reduction of the redox centre to its metallic state. This reduction is accompanied by an exhaustive structural rearrangement, inflicting substantial volume changes (often >100%) and phase segregation [22]. These effects seriously challenge the reversibility of the electrochemical reaction, as the loss of electrode integrity and continuous formation of solid electrolyte interface (SEI) on freshly exposed electrode surface lead to rapid capacity decay and low coulombic efficiency. The low reversibility of alloy and conversion electrode reactions are seen as the main drawback for their penetration into the commercial market. Therefore, monitoring and constraining the morphological changes upon lithiation is of major importance to pave the way for their application as greatly desired high energy density electrodes for rechargeable lithium ion batteries.

Iron-oxide based electrode materials are particularly appealing for large scale electrochemical energy storage due to the electrode material's abundance, environmental benignancy, low-cost and high safety when employed as electrode material [23]. Moreover, Fe_2O_3 haematite can take up to six Li per formula unit in a conversion reaction, resulting in a very high theoretical capacity of 1007 mA h g^{-1} [24]. *Larcher* et al. showed that the lithiation reaction path and its reversibility strongly depend on the morphology of the Fe_2O_3 starting material [25]. Inspired by that study much follow-up work was dedicated to the synthesis of Fe_2O_3 with diverse nanostructures to constrain and buffer the morphological changes in order to extend cycle life, see *Lin* et al. and references there within [26]. Remarkable reversible capacity of up to 877 mA h/g, rate capability up to 20 C and cycling stability of over 1000 cycles have been reported for sophistically tailored Fe_2O_3 nanosheets [27]. As an alternative approach, doping has been reported to increase intrinsically low conductivity of Fe_2O_3 and preserve microstructure by preventing fatal fracturing of nanoscaled electrode [28]. In this regard, enhanced electrochemical performance due to improved charge transfer ability was reported for Mn-doped Fe_2O_3 [29]. Likewise, improved long-term cycling stability of Fe_2O_3 thanks to stress relief from metal dopant buffer for Zn and Co doping was shown [30,31].

Microstructural changes, such as phase segregation, electrode fracturing, nanoparticle growth and agglomeration occurring in conversion type electrode materials upon lithiation are often detrimental for their electrochemical cycling stability. To address this challenge we present here for the first time the application of a combined simultaneous SAXS-XAS technique to the field of battery materials to qualitatively monitor and quantitatively analyse the morphological changes under *operando* conditions.

2. Experimental

2.1. Sample and electrode preparation

The Sr and Ca-doped Fe_2O_3 materials were synthesised via high energy ball-milling of Fe_2O_3 powder with their dopants' respective carbonates. The carbonates were weighed so that the Sr or Ca content corresponded to 12 wt%, powders were inserted into Zr vials and milled in a planetary ball mill for 24 h. The resulting materials were then thoroughly washed using acetic acid to remove any remaining carbonates. The resulting powders were subsequently characterised to ensure phase purity and successful carbonate removal. For the electrodes, active material and carbon black were weighed out at a ratio of 7.5/1.5. These were then further ball-milled under ethanol for 1 h and subsequently dried under vacuum overnight. A PVdF/NMP solution was then added to the mixture so that the PVdF content corresponded to 10 wt%. The slurry was stirred thoroughly before casting onto Cu foil and drying under vacuum. Electrode processing was aimed at optimising spectroscopic results not their electrochemical performance. Specially designed pouch cells were assembled, incorporating Cu-foil windows instead of a full-laminated pouch so as to minimise the background scattering contribution, see scheme in S.I.

2.2. Material characterization

X-ray diffraction patterns were characterised on X-ray diffractometer (XRD, Rigaku, MiniFlex 600) using Cu-Kα radiation. Elemental analysis and mapping were carried out by scanning electron microscopy (SEM, HITACHI, S–3400 N) at 10 kV with energy dispersive X-ray spectroscopy (EDX, Oxford instruments, X-Max).

2.3. Joined operando SAXS - XAS

Specifically designed pouch cells were cycled for two complete electrochemical cycles while being subject to synchrotron radiation in transmission mode for simultaneous acquisition of SAXS and XAS spectra. The experimental details for this joined setup at BM26A Dutch-Belgian Beamline at the European Synchrotron Radiation Facility (ESRF) have been previously described elsewhere [32]. The energy was tuned via a double-crystal monochromator operating in fixed-exit mode equipped with a Si (111) crystal pair. Energy calibration was performed by measuring XAS of iron metal foil. The beamsize was about 1 × 0.5 mm and the acquisition time for SAXS images was 30 s using a 2D Pilatus

Dectris detector. A photodiode was used to acquire absorption spectra, and the acquisition took $\approx$ 15 min per spectra. The 2D SAXS images were integrated, normalized to electronic units and fitted using XRTools and an in-house software [33]. Likewise, XANES spectra were extracted, normalized, aligned, and cleaned using Athena software from Demeter package [34].

3. Results

3.1. Material characterization

The x-ray diffraction pattern of the active electrode material of pure and doped Fe_2O_3 are illustrated in Fig. 1. The three diffraction patterns coincide greatly and all main features can be attributed to the well-documented haematite structure (ICSD 15840) with $R\overline{3}c$ space group [35]. Besides confirming mutual crystal structure, XRD reveals the absence of phase segregation and impurities within the range of sensitivity. The peak broadening was analysed using the Scherrer equation revealing similar crystal domain sizes in the range of 32–36 nm for the three materials. This is expected since crystal domain size is largely defined by mechano-synthesis and heat treatment parameters which are identical for all three samples. Interestingly, the peak positions for doped samples are shifted to higher angles compared to pure Fe_2O_3, see inset Fig. 1. The shift to higher angles indicates a lattice contraction as a result of the creation of oxygen vacancies to maintain electronic neutrality upon substitution of Fe^{3+} by Me^{2+} dopant [31,36]. This along with absence of minority phases, proves the effective incorporation of the dopant into the crystal lattice. The shift is slightly more pronounced for Sr-doped than for Ca-doped Fe_2O_3, which could be linked to slight deviation in doping level, vide infra.

SEM-EDX mapping of casted Sr and Ca-doped electrodes reveal homogeneous distribution of the dopants, see S.I. The doping level was quantified to be $\approx$ 7 and 10 at.% for Ca and Sr, respectively, resulting in the approximate chemical formula of $Me_{0.2}Fe_{1.8}O_{2.9}$, whereas $Me = Sr$ or Ca.

3.2. Operando SAXS-XAS analysis

The *operando* SAXS-XAS electrochemical cycling curves of all three samples follow characteristic signature of micrometer-sized haematite lithiation, see S.I. Upon discharge only a negligible small amount of lithium is reacting at elevated potential of 1.3 V corresponding to monophasic insertion of lithium in a solid solution [23]. This is ensued

Fig. 1. XRD pattern of pure Ca-doped and Sr-doped Fe_2O_3. Inset shows zoom of xrd feature corresponding to (104) plane.

by an extensive plateau centred around 0.8 V which represents the biphasic conversion of Fe_2O_3 to metallic Fe and Li-oxide. Subsequently a sloping curve is observed until the lower voltage cut-off is reached. Among the three samples, Sr-doped Fe_2O_3 has the smallest initial discharge capacity expressed by a shortened conversion plateau and a much steeper decay of the subsequent sloping curve. This suggests that the Sr-doping restrains the conversion of Fe_2O_3 compared to Ca-doped and non doped Fe_2O_3. As the initial discharge reaction comprises major SEI formation and other irreversible reactions, only a part of the inserted charge is recovered upon subsequent delithiation (charge) [23, 30].

Operando Fe K-edge XANES spectra at selected states of charge; pristine, end of first discharge (EOD1), end of first charge (EOC1), end of second discharge (EOD2), as well as *ex situ* end of 10th charge (EOC10) are shown in Fig. 2 for Fe_2O_3 pure (left), Ca-doped (centre) and Sr doped (right), respectively. The absorption Fe K-edge which is susceptible to the oxidation state and coordination of the absorber, reveals similar shape and position for all three pristine materials, well matching the Fe_2O_3 reference spectra (pink dotted line). Furthermore, Extended X-ray Absorption Fine Structure (EXAFS) spectra confirms that all three pristine materials have very similar local structure, resembling closely that of reference haematite see Fig. S5 (top) in S.I.

Upon first discharge (lithiation) the XANES edge shape changes drastically for pure and Ca-doped Fe_2O_3. The white line intensity is strongly reduced and the edge position is shifted to lower energy values, which is in accordance with the reduction of Fe^{+3} to metallic Fe. The predominance of metallic iron at the end first discharge (EOD1) is confirmed by the similarity of the EOD1 spectra to that of Fe metal foil reference (orange dotted line). The small differences between EOD1 and metal reference spectra stem from bulk vs. nanoparticle (NP) confinement of the Fe absorber. EXAFS Fourier transform confirms the effective transformation from oxide to metallic nanoparticle for Ca-doped and pure Fe_2O_3, see Fig. S5 (bottom) in S.I. For the Sr-doped Fe_2O_3 a less pronounced change of the absorption edge is observed upon initial discharge. Analogous to pure and Ca-doped Fe_2O_3, its edge is shifted to lower energy values. However, the shape and position of Sr-doped EOD1 spectra does not resemble that of iron metal but lies between FeO(+II) (grey dotted line) and Fe (0) metal reference. Due to the instability of iron in the monovalent state, no XANES reference pattern are available for fingerprinting this intermediate. Nevertheless, when compared with literature, best agreement of the Sr-doped Fe_2O_3 at EOD1 is found with a spectra of Fe_2O_3 reacted with 4 Li [25]. This implies that Sr-doped Fe_2O_3 is not reduced to metallic state at the end of first discharge, but remains in an average intermediate oxidation state of $\approx$ +I. This incomplete reaction is also reflected by a lower discharge capacity of Sr-doped compared to Ca-doped and non doped Fe_2O_3 see S.I.

Upon inversion of the electrochemical reaction, charge (delithiation) only small changes of the shape and position of the absorption edge occurs for pure and Ca-doped Fe_2O_3, resembling still strongly that of Fe metal reference. This implies that only a small part of the previously formed metallic Fe NP are re-oxidised back to Fe_2O_3. On the contrary, for the Sr-doped material an increase in peak intensity along with a shift of the edge position to higher values is observed upon charge (EOC1). The edge position of Sr-doped Fe_2O_3 coincides well with that of FeO fingerprint, implying an overall oxidation number of $\approx$+2. Although the initial state is not recovered, it is salient that Fe K-edge of EOC1 of Sr-doped resembles much more that of pristine state than for pure and Ca-doped Fe_2O_3 spectra. This hints an increased reversibility of the electrochemical reaction of the former. Nevertheless, at the end of second discharge (lithiation), all three Fe_2O_3 samples reveal similar edge shapes and positions resembling strongly that of metallic Fe. This suggests that the peculiarity of Sr-doped material observed during first discharge (EOD1) is not maintained during the subsequent cycles. This is furthermore confirmed by *ex situ* XANES spectra after 10 complete cycles (EOC10) revealing similar edge shape for all three samples, closely coinciding with that of metal iron reference.
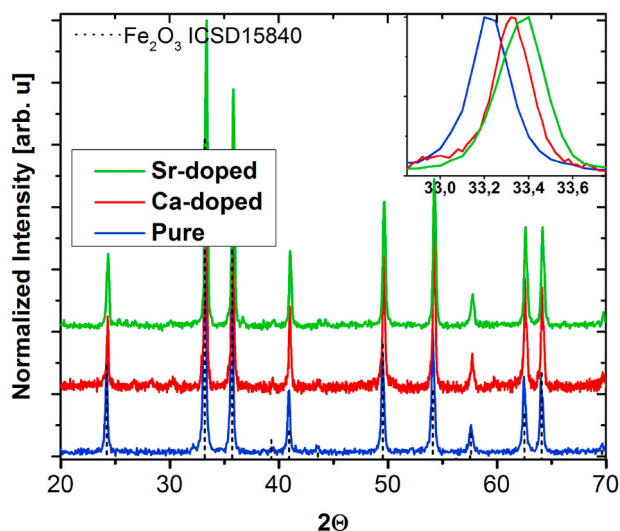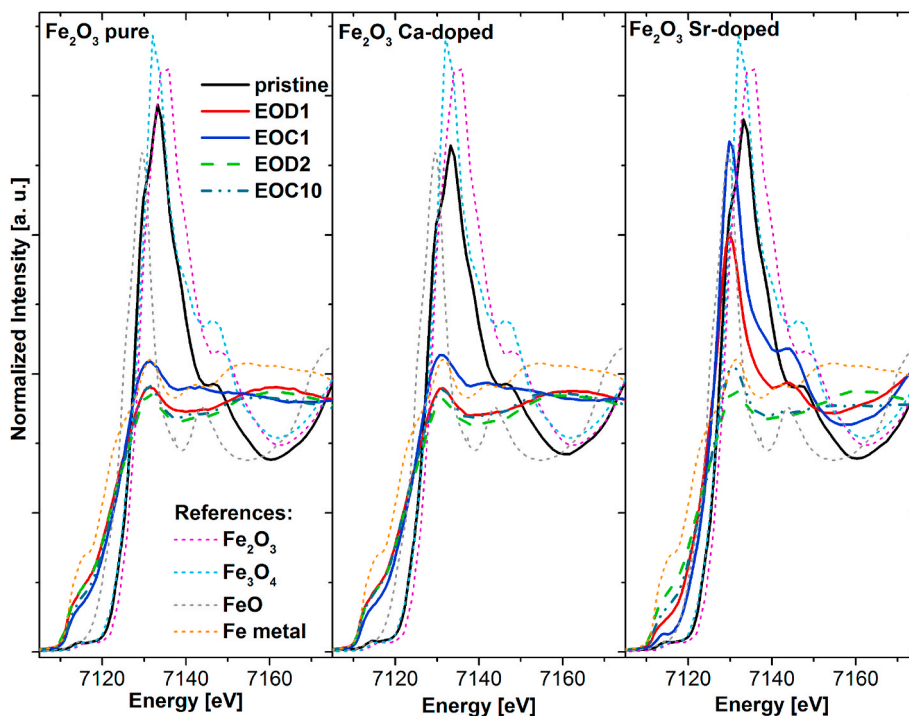
Fig. 2. XANES spectra at selected points during electrochemical cycling; pristine, end of first discharge (EOD1), end of first charge (EOC1), end of second discharge EOD2, as well as *ex situ* end of 10th charge (EOC10) for pure (left), Ca-doped (center), and Sr-doped (right) Fe₂O₃, respectively. Dotted lines are fingerprint spectra of Fe₂O₃, Fe₃O₄, FeO and Fe metal foil references.

To follow the morphological changes of the Fe₂O₃ electrodes upon electrochemical cycling, small angle x-ray scattering spectra were acquired simultaneous along with x-ray absorption spectra under *operando* conditions. The scattering curves at distinct points of the electrochemical cycling, are depicted in Fig. 3 for pure (left), Ca-doped and Sr-doped Fe₂O₃, respectively. The background spectra (dotted orange line) which contains combined scattering contribution of the air gap and all cell components except the active material Fe₂O₃ proves that main scattering contribution originates from active electrode material.

Analogous to the XANES spectra, the SAXS spectra of all three electrodes at pristine state are very similar. This confirms comparable morphology and microstructure of the active material before electrochemical reaction. The absence of a plateau in the low q region indicates the presence of large mesoscaled entities which are so large (micrometer size) that the experimentally observed q range depicts only the tail of their scattering contribution. Upon first discharge the scattering intensity is reduced in the low q region (Porod) along with the formation of a hump in the region of $1–3\ \text{nm}^{-1}$. The observed decrease in scattering
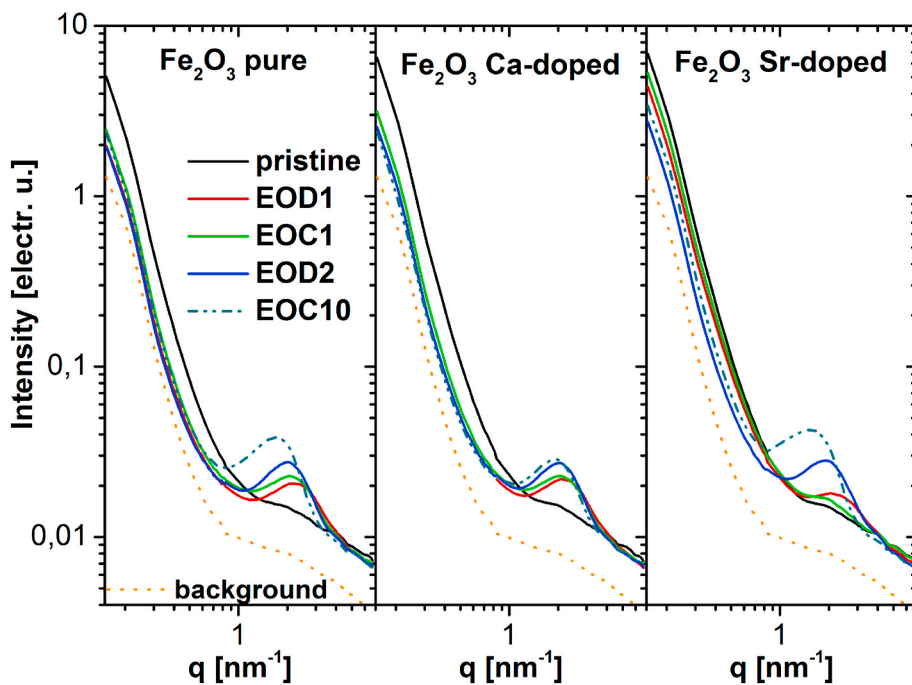
Fig. 3. SAXS spectra at selected states of charge; pristine, end of first discharge (EOD1), end of first charge (EOC1), end of second discharge EOD2 as well as *ex situ* end of 10th discharge for pure, Ca-doped, and Sr-doped Fe₂O₃ right, centre and left, respectively. Dotted orange line background spectra contains combined scattering contribution of air gap and all cell components except Fe₂O₃ active anode material. (For interpretation of the references to colour in this figure legend, the reader is referred to the Web version of this article.)

intensity in the Porod region can be attributed to changes of this mesoscale structure, in line with the fracturing of the bulk electrode.

The formation of a broad hump in the high q region (2-3 nm^{-1}) points towards the formation of nanoparticles. It is noteworthy that these changes are far less pronounced for Sr-doped than for the other two Fe$_2$O$_3$ samples, suggesting a greater degree of morphological preservation in the former. Moreover, these changes are partially reversible upon charge (relithiation) for Sr-doped Fe$_2$O$_3$, contrary to pure and Ca-doped Fe$_2$O$_3$. For the later, a slight increase of hump intensity is observed upon charge. This is well in line with the observation of enhanced reversibility for Sr-doped Fe$_2$O$_3$ from XANES analysis see Fig. 2. Nevertheless, after the second discharge (EOD2) a similar small-angle scattering spectra were obtained for all three samples, suggesting that the preservation of morphology is not maintained during second discharge. The *ex situ* sample after 10 complete cycles reveals a further increase in hump intensity along with a shift to lower q values, which indicates a continuous growth in average size of the scattering objects. It is noted that this continuous growth is less pronounced for Ca-doped sample than for the other two, for reasons not certain at this point. The contribution of thin surface layer (e.g. SEI) to the total scattering signal can be considered as negligible due its small volume fraction compared to total electrode thickness.

For enhanced comparability and traceability of the evolution of electronic structure and morphology during the first 1,5 electrochemical cycles vs. lithium, the complete *operando* data set of simultaneously acquired XANES and SAXS spectra are plotted as contour plots for pure and Sr-doped Fe$_2$O$_3$, see Figs. 4 and 5. The plot of Ca-doped is very similar to that of pure Fe$_2$O$_3$ and is presented in the S.I.

The XANES plots reveal a gradual shift to lower energy values followed by a rapid fading of the white line intensity upon initial discharge. At the same time the emerging of a hump in the high q range can be observed in the SAXS spectra. While this evolution is largely irreversible in the case of pure Fe$_2$O$_3$ (see Fig. 4) it is salient that for Sr-doped Fe$_2$O$_3$ (see Fig. 5) both the electronic structure and the morphological changes are much more reversible during 1st charge. Although the pristine state of Sr-doped Fe$_2$O$_3$ is not recovered after one complete cycle (#38), it is evident that the K-edge intensity is strongly increased and the intensity of the hump in the q range 1–3 nm^{-1} is decreased, compared to the end of initial discharge (#23). To illustrate the diverging evolution of SAXS signal of pure and Sr-doped Fe$_2$O$_3$ upon first electrochemical cycle a 3D plot comparing both data set is presented in Fig. S7 in S.I.

3.3. SAXS fitting

In order to analyse the morphological changes quantitatively, *operando* SAXS spectra at distinct points of electrochemical cycling were fitted to obtain characteristic parameters of the microstructure, see S.I. for SAXS fits and further details. The evolution of the particle radius (top), packing density (center), and Porod scattering intensity (bottom) are presented in Fig. 6.

The top graph illustrates that the average size of the mono-dispersed spherical scattering objects gradually increases for pure and Ca-doped Fe$_2$O$_3$ upon electrochemical cycling. This reflects the formation metallic iron nanoparticles as evinced by XAS. For Sr-doped Fe$_2$O$_3$ however, the particle size growth is less intense during the first discharge and is even reduced after one complete cycle, reflecting the enhanced reversibility of Fe NP formation. At the completion of the second electrochemical cycle the particle size for Sr-doped sample increases strongly and reaches comparable value as for other two samples suggesting similar nanoparticles presence. The fact that particle size of *ex situ* spectra (EOC10) is higher than that of EOD2 for all three samples points towards a continuous growth or agglomeration of metallic iron nanoparticles upon subsequent cycling. The packing density (or fraction) parameter η, which can range from 0 to 0.74, reflects the structure factor contribution originating from particle scattering interference. At pristine state η is close to zero, indicating that scattering particles are so far from each other that no scattering interference occurs. Analogous to the trend of the particle size evolution, η is strongly increasing for Ca-doped and pure Fe$_2$O$_3$ upon first discharge, whereas for Sr-doped Fe$_2$O$_3$ the packing density increases less strongly. The observed rise in packing density η is in good agreement with the formation of iron nanoparticle, which result in a surge of particle interaction. Upon subsequent charge, η is effectively reduced for the Sr-doped Fe$_2$O$_3$, while it remains constant at an elevated level for the other two samples. The second discharge shows an increase of particle interference for all samples, with the Sr-doped sample attaining a similar level as the other two samples. Last but not least, the evolution of the scattering intensity in the Porod region is illustrated in Fig. 6 (bottom). This parameter indirectly reflects the changes in the mesoscopic morphology of the electrodes. While for pure and Ca-doped Fe$_2$O$_3$ a sharp drop upon initial discharge followed by a plateauing is observed, a less severe reduction is found for Sr-doped sample which is followed by a slight increase at EOC1. This illustrates that the mesoscale structural changes for Ca-

Fig. 4. Evolution of simultaneously acquired *operando* Fe K-edge XANES (left) and SAXS (right) during first 1,5 electrochemical cycles of pure Fe$_2$O$_3$ vs. Li.

Fig. 5. Evolution of simultaneously acquired *operando* Fe K-edge XANES (left) and SAXS (right) during first 1,5 electrochemical cycles of Sr-doped Fe$_2$O$_3$ vs. Li.

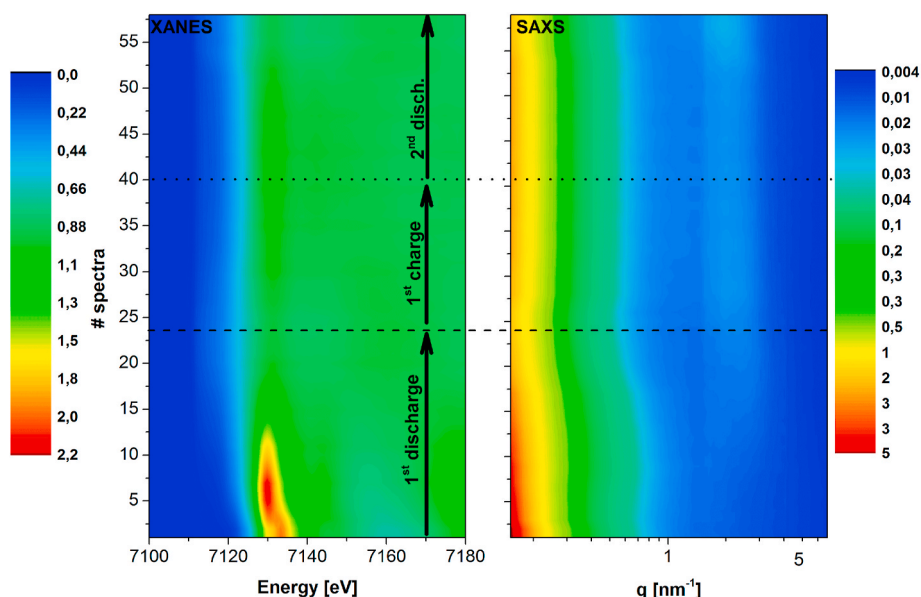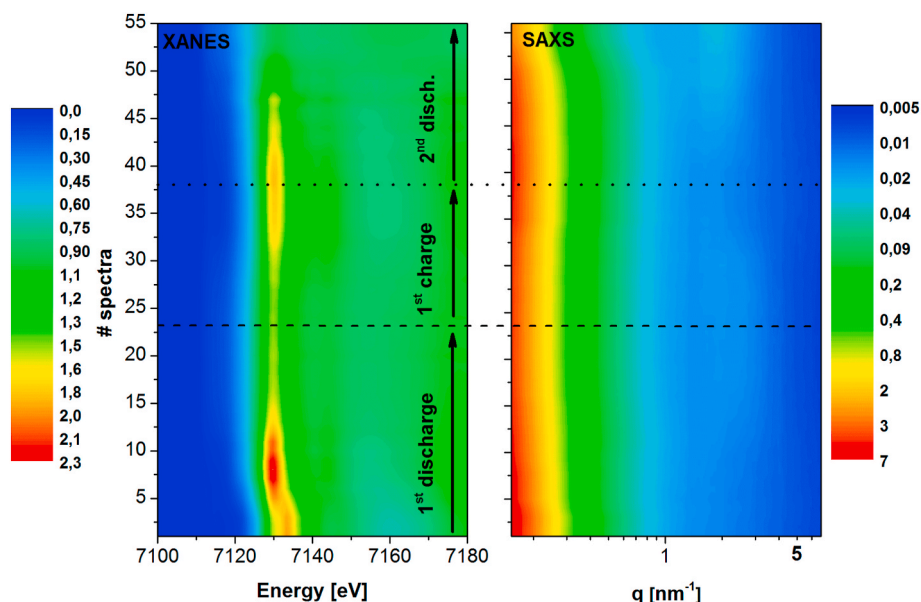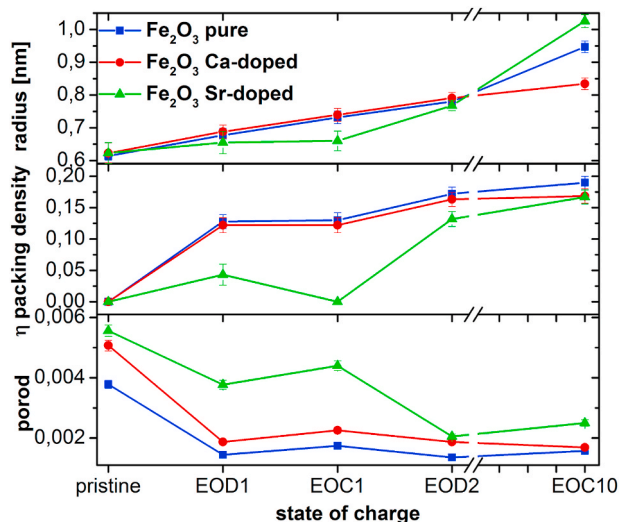**Fig. 6.** Fitting parameters of particle size (top), packing density (center), and Porod scattering intensity (bottom) of SAXS spectra at distinct points of charge; pristine, end of first discharge (EOD1), end of first charge (EOC1), end of second discharge (EOD2), as well as *ex situ* end of 10th discharge for pure (blue), Ca-doped (red), and Sr-doped (green) Fe$_2$O$_3$, respectively. (For interpretation of the references to colour in this figure legend, the reader is referred to the Web version of this article.)

doped and pure Fe$_2$O$_3$ upon initial lithiation are further-reaching and less reversible than for Sr-doped Fe$_2$O$_3$. However, analogous to particle size and packing density, similar values are found for the Porod parameter beyond EOC1. This suggests that the mesostructures of all three Fe$_2$O$_3$ samples are converging after completion of the first electrochemical cycle.

4. Discussion

The combined simultaneous *operando* XANES-SAXS measurement provides a comprehensive picture of morphological, electronic and local structural transformations upon lithiation of Fe$_2$O$_3$. The *operando* conditions assure a high reliability, and consistency, as well as a low sample bias of the findings. Element specific XANES reveals that upon initial

discharge, iron is effectively reduced to metallic Fe nanoparticles, accompanied by strong changes of the electrode morphology on the meso- and nanostructural scale, evidenced by SAXS. Upon delithiation this reaction is only partially reversed. Interestingly, the degree of reversibility differs strongly for the three examined samples within the first electrochemical cycle. A comparison of the lithiation/delithiation reaction of the three samples Sr-doped, Ca-doped and pure Fe$_2$O$_3$ electrode reveals that the Sr-doped Fe$_2$O$_3$ shows improved reversibility in terms of electronic and morphological structure compared to the other two electrodes. These findings suggest that Sr-doping has a beneficial effect on the reversibility of the conversion reaction by effectively suppressing changes of mesoscopic and nanoscopic structure. A tentative explanation could be an increased capability of Sr-doped Fe$_2$O$_3$ to store lithium via intercalation mechanism rather than conversion mechanism, which imposes less severe structural transformation. However, the electrochemical signature of Sr-doped Fe$_2$O$_3$ does not indicate a more pronounced solid-solution behaviour. A more likely scenario is the stabilising effect of Sr-doping on the Fe$_2$O$_3$ structure, impeding its complete decomposition upon lithiation. This is in line with the observed reduced capacity of the first discharge of Sr-doped Fe$_2$O$_3$. In this way it preserves the electrode material from profound structural changes which facilitates the delithiation reaction. This is a well-known strategy for enhancing reversibility in alloy-type electrodes [37]. Another beneficial aspect of Sr-doping could be its potential role as an electrochemically inactive mitigator, preventing nanoparticle aggregation and acting as a structural anchor point, hence promoting the re-oxidation reaction, analogous to titanium in the conversion reaction of TiSnSb vs. Li [38]. The fact that the enhanced reversibility of Sr-doped Fe$_2$O$_3$ is lost after the first cycle, underlines the need for further optimisation and material tailoring studies. As previously stressed, controlling the particle size and preserving electrode morphology and integrity is of crucial importance for the cyclability of conversion electrode materials such as haematite. The here for the first time applied combined simultaneous SAXS-XAS technique provides valuable, qualitative and quantitative insights on the structural and morphological changes under real cycling conditions, thus pinpointing possible ways to mitigate and alleviate their detrimental effects. In this regard, the here presented confinement of microstructure and morphology via Sr-doping is an interesting mean to improve the low reversibility of Fe$_2$O$_3$, albeit at the cost of slightly reduced total capacity. While in this study the simultaneous *operando* SAXS-XAS was demonstrated on the example of a metal oxide anode, it is

expected that the technique can be applied to a wide range of conversion and alloy type electrode materials and for different battery chemistries.

5. Conclusion

In this study, we present a combined *operando* SAXS-XAS technique, for the first time applied in the field of battery electrode materials. This approach enabled us to follow simultaneously the electronic, morphological, local and mesostructural changes under *operando* conditions on the example of the conversion reaction of Fe_2O_3's lithiation. While SAXS enabled us to closely monitor and quantify the structural changes, XANES allowed their precise attribution to the state of charge of the redox-active electrode material. The exhaustive data set reveals, that the lithiation reaction is accompanied by the formation of iron nanoparticles, inflicting strong morphological changes. By comparing Fe-samples of different dopants, we show that the degree of reversibility of the conversion reaction is increased for Sr-doped compared to pure and Ca-doped Fe_2O_3 thanks to restraining of the microstructure and the degree of discharge. The comprehensive insights obtained by this joined technique provide a holistic picture of the structural changes of the conversion electrode material under realistic conditions. Combined SAXS-XAS is therefore a useful tool for deeper understanding of alloy and conversion type electrode materials of different battery chemistries, paving the way for adequate material tailoring solutions.

CRediT authorship contribution statement

Marcus Fehse: Investigation, Formal analysis, Writing - original draft. **Matteo P. Hogan:** Resources, Investigation. **Sally Hiu-Tung Pang:** Formal analysis. **Oliver Blackman:** Resources, Investigation. **Erik M. Kelder:** Funding acquisition, Supervision. **Alessandro Longo:** Investigation, Writing - original draft, Supervision. **Maria Alfredsson:** Investigation, Funding acquisition, Supervision.

Declaration of competing interest

The authors declare that they have no known competing financial interests or personal relationships that could have appeared to influence the work reported in this paper.

Acknowledgements

Appendix A. Supplementary data

Scheme of *operando* cell assembly, electrochemical cycling curve, SEM micrographs and elemental mapping, EXAFS Fourier transform of pristine state and EOD1 state, contour plot of Ca-doped XANES and SAXS, 3D plot of SAXS pure vs. Sr-doped Fe_2O_3 and fitting of Sr-doped Fe_2O_3 SAXS spectra at specific points of electrochemical cycling.

Supplementary data to this article can be found online at https://doi.org/10.1016/j.jpowsour.2020.228685.

References

[1] Z. Gong, Y. Yang, J. Energy Chem. 27 (2018) 1566–1583, https://doi.org/10.1016/j.jechem.2018.03.020. https://www.sciencedirect.com/science/article/pii/S2095495617311877?{_}rdoc=1{&}{_}fmt=high{&}{_}origin=gateway{&}{_}docanchor={&}md5=b8429449ccfc9c30159a5f9aeaa92ffb{&}dgcid=raven{_}sd{_}recommender{_}email.

[2] M. Fehse, A. Iadecola, M.T. Sougrati, P. Conti, M. Giorgetti, L. Stievano, Energy Storage Mater 18 (2019) 328–337, https://doi.org/10.1016/j.ensm.2019.02.002. https://www.sciencedirect.com/science/article/pii/S2405829719300431.

[3] D. Puthusseri, M. Wahid, S. Ogale, ACS Omega 3 (2018) 4591–4601, https://doi.org/10.1021/acsomega.8b00188.

[4] M. Fehse, M.T. Sougrati, A. Darwiche, V. Gabaudan, C. La Fontaine, L. Monconduit, L. Stievano, J. Mater. Chem. 6 (2018) 8724–8734, https://doi.org/10.1039/c8ta02248h. http://pubs.rsc.org/en/Content/ArticleLanding/2018/TA/C8TA02248H.

[5] L. Wang, J. Wang, P. Zuo, Small Methods 2 (2018) 1700293, https://doi.org/10.1002/smtd.201700293. _eprint: https://onlinelibrary.wiley.com/doi/pdf/10.1002/smtd.201700293, https://onlinelibrary.wiley.com/doi/abs/10.1002/smtd.201700293.

[6] H.J.G. Malabet, D.J. Robles, V.d. Andrade, P.P. Mukherjee, G.J. Nelson, J. Electrochem. Soc. 167 (2020), 040523. https://doi.org/10.1149/1945-7111/ab78fb. doi:10.1149/1945-7111/ab78fb, publisher: The Electrochemical Society.

[7] C. Lamberti, G. Agostini, Characterization of Semiconductor Heterostructures and Nanostructures, C, Elsevier, Torino, (2013) doi:10.15713/ins.mmj.3. arXiv:arXiv:1011.1669vol. 3.

[8] Y. Ren, X. Zuo, Small Methods (2018) 1–19, https://doi.org/10.1002/smtd.201800064, 1800064.

[9] J. Conder, C. Marino, P. Novak, C. Villevieille, J. Mater. Chem. (2018), https://doi.org/10.1039/C7TA10622J. http://pubs.rsc.org/en/Content/ArticleLanding/2018/TA/C7TA10622J.

[10] D.A. Stevens, J.R. Dahn, J. Electrochem. Soc. 147 (2000) 4428–4431, https://doi.org/10.1149/1.1394081. http://jes.ecsdl.org/cgi/doi/10.1149/1.1394081.

[11] G. Sandí, H. Joachin, R. Kizilel, S. Seifert, K.A. Carrado, Chem. Mater. 15 (2003) 838–843, https://doi.org/10.1021/cm020670z.

[12] S. Komaba, W. Murata, T. Ishikawa, N. Yabuuchi, T. Ozeki, T. Nakayama, A. Ogata, K. Gotoh, K. Fujiwara, Adv. Funct. Mater. 21 (2011) 3859–3867, https://doi.org/10.1002/adfm.201100854, arXiv:0706.1062v1.

[13] V. Simone, A. Boulineau, A. de Geyer, D. Rouchon, L. Simonin, S. Martinet, J. Energy Chem. 25 (2016) 761–768, https://doi.org/10.1016/j.jechem.2016.04.016. http://www.sciencedirect.com/science/article/pii/S2095495616300535{#}fig0002.

[14] G. Möhl, E. Metwalli, P. Muller-Buschbaum, ACS Energy Lett 3 (2018) 1525–1530, https://doi.org/10.1021/acsenergylett.8b00763.

[15] D. Saurel, J. Segalini, M. Jauregui, A. Pendashteh, B. Daffos, P. Simon, M. Casas-Cabanas, Energy Storage Mater 21 (2019) 162–173, https://doi.org/10.1016/j.ensm.2019.05.007.

[16] P. Ranque, C. George, R.K. Dubey, R. van der Jagt, D. Flahaut, R. Dedryvère, M. Fehse, P. Kassanos, W.F. Jager, E.J.R. Sudholter, E.M. Kelder, ACS Appl. Energy Mater. 3 (2020) 2271–2277, https://doi.org/10.1021/acsaem.9b01225. https://pubs.acs.org/doi/10.1021/acsaem.9b01225.

[17] K.M. Wiaderek, O.J. Borkiewicz, N. Pereira, J. Ilavsky, G.G. Amatucci, P.J. Chupas, K.W. Chapman, J. Am. Chem. Soc. 136 (2014) 6211–6214, https://doi.org/10.1021/ja501854y. http://pubs.acs.org/doi/abs/10.1021/ja501854y.

[18] G.O. Park, J. Yoon, E. Park, S.B. Park, H. Kiim, K.H. Kim, X. Jin, T.J. Shin, H. Kim, W.S. Yoon, J.M. Kim, ACS Nano 9 (2015) 5470–5477, https://doi.org/10.1021/acsnano.5b01378. http://pubs.acs.org/doi/abs/10.1021/acsnano.5b01378.

[19] J.K. Shon, H.S. Lee, G.O. Park, J. Yoon, E. Park, G.S. Park, S.S. Kong, M. Jin, J.-M. Choi, H. Chang, S. Doo, J.M. Kim, W.-S. Yoon, C. Pak, H. Kim, G.D. Stucky, Nat. Commun. 7 (2016) 11049, https://doi.org/10.1038/ncomms11049. https://www.ncbi.nlm.nih.gov/pmc/articles/PMC4804172/pdf/ncomms11049.pdfΩhttp://www.nature.com/ncomms/2016/160322/ncomms11049/full/ncomms11049.html.

[20] G.O. Park, J. Yoon, J.K. Shon, Y.S. Choi, J.G. Won, S.B. Park, K.H. Kim, H. Kim, W.S. Yoon, J.M. Kim, Adv. Funct. Mater. 26 (2016) 2800–2808, https://doi.org/10.1002/adfm.201600121.

[21] S.M. Bhaway, Z. Qiang, Y. Xia, X. Xia, B. Lee, K.G. Yager, L. Zhang, K. Kisslinger, Y.M. Chen, K. Liu, Y. Zhu, B.D. Vogt, ACS Nano 11 (2017) 1443–1454, https://doi.org/10.1021/acsnano.6b06708. http://pubs.acs.org/doi/abs/10.1021/acsnano.6b06708.

[22] J. Cabana, L. Monconduit, D. Larcher, M.R. Palacín, Adv. Mater. 22 (2010), https://doi.org/10.1002/adma.201000717. E170–92, http://www.ncbi.nlm.nih.gov/pubmed/20730811.

[23] J. Hassoun, F. Croce, I. Hong, B. Scrosati, Electrochem. Commun. 13 (2011) 228–231, https://doi.org/10.1016/j.elecom.2010.12.020. https://www.sciencedirect.com/science/article/pii/S1388248110005412.

[24] O.J. Borkiewicz, B. Shyam, K.M. Wiaderek, C. Kurtz, P.J. Chupas, K.W. Chapman, J. Appl. Crystallogr. 45 (2012) 1261–1269, https://doi.org/10.1107/S0021889812042720. http://scripts.iucr.org/cgi-bin/paper?S0021889812042720.

[25] D. Larcher, D. Bonnin, R. Cortes, I. Rivals, L. Personnaz, J.-M. Tarascon, J. Electrochem. Soc. 150 (2003) A1643, https://doi.org/10.1149/1.1622959. http://jes.ecsdl.org/cgi/doi/10.1149/1.1622959.

[26] Y.M. Lin, P.R. Abel, A. Heller, C.B. Mullins, J. Phys. Chem. Lett. 2 (2011) 2885–2891, https://doi.org/10.1021/jz201363j. http://pubs.acs.org/doi/10.1021/jz201363j.

[27] K. Cao, L. Jiao, H. Liu, Y. Liu, Y. Wang, Z. Guo, H. Yuan, Adv. Energy Mater. 5 (2015) 1401421, https://doi.org/10.1002/aenm.201401421.

[28] M.S. Balogun, Z. Wu, Y. Luo, W. Qiu, X. Fan, B. Long, M. Huang, P. Liu, Y. Tong, J. Power Sources 308 (2016) 7–17, https://doi.org/10.1016/j.jpowsour.2016.01.043. https://www.sciencedirect.com/science/article/pii/S037877531630043X.

[29] X. Liu, C. Zhao, F. Feng, F. Yu, W. Kang, Q. Shen, RSC Adv. 5 (2015) 7604–7610, https://doi.org/10.1039/c4ra12809e. http://xlink.rsc.org/?DOI=C4RA12809E.

[30] G. Li, X. Xu, R. Han, J. Ma, CrystEngComm 18 (2016) 2949–2955, https://doi.org/10.1039/c5ce02408k. http://xlink.rsc.org/?DOI=C5CE02408K.

[31] H. Kong, C. Lv, C. Yan, G. Chen, Inorg. Chem. 56 (2017) 7642–7649, https://doi.org/10.1021/acs.inorgchem.7b00008. http://pubs.acs.org/doi/10.1021/acs.inorgchem.7b00008.

[32] A.M. Beale, A.M. Van Der Eerden, S.D. Jacques, O. Leynaud, M.G. O'Brien, F. Meneau, S. Nikitenko, W. Bras, B.M. Weckhuysen, J. Am. Chem. Soc. 128 (2006) 12386–12387, https://doi.org/10.1021/ja062580r. https://pubs.acs.org/doi/10.1021/ja062580r.

[33] P. Calandra, A. Longo, V.T. Liveri, J. Phys. Chem. B 107 (2003) 25–30, https://doi.org/10.1021/jp021223+. http://pubs.acs.org/doi/abs/10.1021/jp021223%5c%5c%5c%5c2B?journalCode=jpcbfk.

[34] B. Ravel, M. Newville, in: J. Synchrotron Radiat, vol. 12, Munksgaard International Publishers, 2005, pp. 537–541, https://doi.org/10.1107/S0909049505012719. http://scripts.iucr.org/cgi-bin/paper?S0909049505012719.

[35] R.L. Blake, Hessevic Re, T. Zoltai, L.W. Finger, Am. Mineral. 51 (1966) 123–129, https://doi.org/10.1158/1538-7445.AM2011-83.

[36] C. Lopez, C. Baroni, J.M. Tulliani, Materials 6 (2013) 4801–4816, https://doi.org/10.3390/ma6104801. http://www.mdpi.com/1996-1944/6/10/4801.

[37] J.R. Szczech, S. Jin, Energy Environ. Sci. 4 (2011) 56–72, https://doi.org/10.1039/c0ee00281j.

[38] M. Fehse, A. Darwiche, M.T. Sougrati, E.M. Kelder, A.V. Chadwick, M. Alfredsson, L. Monconduit, L. Stievano, Chem. Mater. 29 (2017) 10446–10454, https://doi.org/10.1021/acs.chemmater.7b04088. http://pubs.acs.org/doi/10.1021/acs.chemmater.7b04088.